Two-Dimensional White-Light Spectroscopy

Using Supercontinuum from an All-Normal

Dispersion Photonic Crystal Fiber Pumped by a

70 MHz Yb Fiber Oscillator

Nicholas M. Kearns, Andrew C. Jones, Miriam Bohlmann Kunz, Ryan T. Allen, Jessica T.

Flach, and Martin T. Zanni*

Department of Chemistry, University of Wisconsin – Madison, 1101 University Ave.

Madison, Wisconsin, 53706, United States

*Corresponding Author

zanni@chem.wisc.edu

(608) 262-4783

Abstract

We report on a new broadband, ultrafast two-dimensional white-light (2DWL) spectrometer that utilizes a supercontinuum pump and a supercontinuum probe generated with a ytterbium fiber oscillator and an all-normal dispersion photonic crystal fiber (ANDi PCF). We demonstrate compression of the supercontinuum to sub-20 fs and the ability to collect high quality 2D spectra on films of single-walled carbon nanotubes. Two spectrometer designs are investigated. Supercontinuum from ANDi PCF provides a means to generate broadband pulse sequences for multidimensional spectroscopy without the need for an optical parametric amplifier.

1. Introduction

Broadband two-dimensional electronic spectroscopy (2DES) has been used to uncover information about electronic couplings, ultrafast dynamics, and energy transfer in many materials and condensed phase systems¹⁻⁸. Most 2D experiments employ non-collinear optical parametric amplifiers (NOPAs)⁹ to obtain spectral coverage throughout the visible and near-infrared region of the electromagnetic spectrum. It is also common to utilize a NOPA pump followed by a whitelight continuum probe^{10,11}. Additionally, there are also broadband 2D electronic spectrometers that do not utilize a NOPA at all, but instead use continuum generated either in gas^{12,13} or pressurized gas-filled fibers¹⁴⁻¹⁶. We have begun using white-light generated in bulk media like YAG, sapphire, and CaF₂ for both the pump and the probe pulses in 2D spectroscopy^{3,17,18}, as has been used for many years to generate broadband probe pulses in transient absorption spectroscopy^{19–21}. We call this approach 2D White-Light (2DWL) spectroscopy. White-light is straightforward to generate in this manner but necessitates an amplified laser source with ~1 µJ-level pulse energy for bulk-materials and hundreds of μJ for continuum in gas²². Thus, whether using a NOPA or WL as a pump, the majority of 2D electronic spectrometers are based on amplified laser systems. In this article, we report a 2D White-Light spectrometer that does not require an amplified laser source by using an all-normal dispersion photonic crystal fiber (ANDi PCF) to generate the supercontinuum.

Nonlinear photonic crystal fibers (PCFs) have been used extensively for supercontinuum generation. The most common types of nonlinear PCF have a zero-dispersion wavelength and exhibit anomalous dispersion on one side of the zero-dispersion wavelength and normal dispersion on the other. By pumping in the anomalous dispersion regime, soliton fission from a high order soliton leads to extreme spectral broadening at relatively low pump peak powers of 1-10 kW^{23,24}.

The resulting supercontinuum is very structured both spectrally and temporally and the pulse-topulse fluctuations can be unsatisfactorily low due to noise from soliton fission^{25–27}. One method of suppressing soliton fission and thereby improving pulse-to-pulse coherence is to generate coherent supercontinua using a PCF with two zero-dispersion wavelengths²⁸. Compressed supercontinuum generated in this type of fiber has been successfully implemented in both coherent anti-Stokes Raman²⁹ and transient absorption³⁰ microscopy. Alternatively, soliton fission can be avoided by pumping in the normal dispersion regime at the cost of output spectral bandwidth²³. Highly coherent, octave-spanning spectra have been generated in all-normal dispersion (ANDi) PCF³¹. Besides all-normal dispersion, ANDi PCF have a flat dispersion profile near the maximum dispersion wavelength. Supercontinuum generation in ANDi PCF results in less spectral broadening than when pumping in the anomalous dispersion regime, but the supercontinuum is highly coherent and reasonably smooth spectrally and temporally, which makes it an attractive source for ultrafast experiments^{31–33}. Several experiments have successfully demonstrated the compression of supercontinuum from ANDi PCF down to sub 10-fs³⁴⁻³⁷. Supercontinuum via PCF is widely used in nonlinear and ultrafast spectroscopy, but we believe that this is the first report using the compressed output of ANDi PCF and the first time that 2D spectroscopy has been performed using PCF of any type.

In this paper, we demonstrate two designs of 2DWL spectrometer, each of which uses supercontinuum generated from ANDi PCF pumped by a Yb fiber oscillator. We demonstrate 2DWL data collection in the visible and near infrared (NIR) region of the electromagnetic spectrum. Using only chirped mirrors to compress the pulse, we achieve 12 fs full-width at half-maximum (FWHM) pulses in the NIR and 18 fs FWHM in the visible. The spectrometers generate

2DWL spectra in the pump-probe geometry³⁸ using variations of a Babinet-Soleil compensator^{39–41}. The spectrometer is demonstrated on thin films of semiconducting carbon nanotubes (CNTs).

2. Experimental methods

2.1 Spectrometer layout

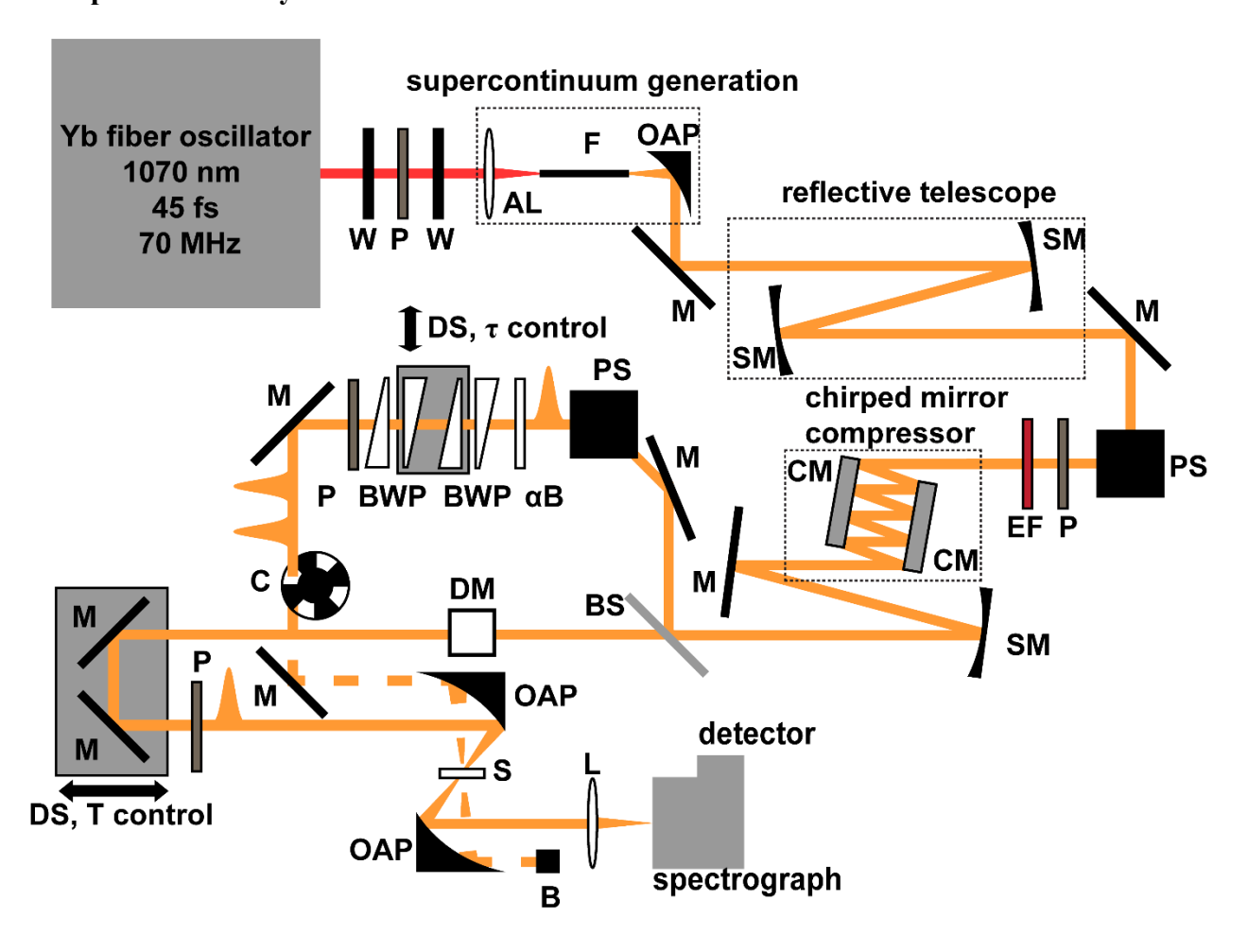


Figure 1. Diagram of experimental layout of 2DWL spectrometer. W: half-wave plate, P: polarizer, AL: aspheric lens, F: ANDi PCF, OAP: 90° off-axis parabolic mirror, M: mirror, SM: spherical mirror, PS: periscope, EF: edge-pass filter, CM: chirped mirror, BS: beam splitter, αB: α-BBO plate, BWP: α-BBO wedge pair, DS: delay stage, C: optical chopper, DM: dispersive material, S: sample, B: beam block, L: lens.

The experimental layout is shown in Figure 1. The output of a Yb fiber oscillator (Coherent Fidelity, 1070 nm, 45 fs, 70MHz, 2.2 W) passes through a half-wave plate and polarizer to attenuate the power followed by a second half-wave plate to control its polarization. An aspheric

lens (8 mm focal length) couples the laser output into a ~5 cm long piece of ANDi PCF (NEG-1050-NL, NKT Photonics) to generate supercontinuum. Previous studies have shown that the broadening of the input spectrum increases with increasing input peak power³². The laser has a built-in prism compressor to pre-compensate for dispersive optics and we adjusted it to optimize for the broadest output spectrum, meaning the pulse is as short as possible at the fiber. The output is collimated with a 90° off-axis parabolic mirror (15 mm reflected focal length). We define the coupling efficiency as the measured power directly after collimation relative to power measured immediately before the aspheric lens. In this work, coupling efficiencies of 35-40% were readily achieved. The collimated supercontinuum was directed into a reflective telescope consisting of two spherical curved mirrors (300 mm and 50 mm focal lengths) to reduce the spot size by a factor of 6. The ANDi PCF is not polarization maintaining, so there is some depolarization of the output relative to the input pulse⁴². A periscope and polarizer are used to rotate and clean the supercontinuum polarization such that it is horizontal. An edge-pass filter with a cutoff wavelength dependent on the spectral range of the experiment filters the pulse spectrum. A pair of chirped mirrors (Laser Quantum) designed to correct for the dispersion of 4.4 mm of CaF₂ per pair of bounces from 600 – 1200 nm compensates for most of the dispersion in path. A long focal length spherical curved mirror (500 mm focal length) is used to gently focus the beam through the rest of the spectrometer and keep the spot size reasonably small. An 80/20 broadband beam splitter (Layertec Gmbh) splits the pulse into the pump (80 %) and probe (20 %). Another periscope rotates the pump polarization by 45°. A modified Babinet-Soleil compensator is used to create a pair of collinear pump pulses separated by a time delay, τ, using a sequence of an α-BBO plate followed by two pairs of α -BBO wedges³⁹⁻⁴¹. The pump pulses are modulated at 500 Hz using a chopper. To match the dispersion from the α -BBO wedges on the pump pulses, the probe is

transmitted through a CaF₂ window, fused silica window, and a single pair of α -BBO wedges to finely adjust the probe dispersion. The pump-probe delay, T, is controlled using an optical delay line on a linear translation stage and a polarizer is used to control the polarization of the probe. The pump and probe are both focused onto the sample with a 90° off-axis parabolic mirror (50 mm reflected focal length), the pump is blocked after the sample, and the probe is dispersed in a spectrograph (SpectraPro 2150, Princeton Instruments) onto a linear InGaAs image sensor (Entwicklungsbüro Stresing). Data from the detector is read at 1 kHz with an integration time of 900 μ s. To keep from saturating the detector, neutral density filters are used after the sample to attenuate the light entering the spectrograph and detector. To remove pump scatter, the position of the final pump mirror was modulated to wash out spectral interference between the pump and probe at the detector⁴³.

To collect a 2D spectrum, a pair of collinear pump pulses separated by delay τ interact with the sample. After time T, a probe pulse interacts with the sample and is dispersed in a spectrograph onto a linear sensor array. To remove the background of the probe spectrum, the pump pulses are modulated with an optical chopper and the change in optical density is calculated. Since we calculate the signal as a change in optical density induced by the pump, ground state bleach (GSB) and stimulated emission (SE) signals are negative, and excited state absorption (ESA) signals are positive. Because the pump pulses cannot be modulated independently, the transient absorption background from each individual pump pulse must be subtracted at each probe pixel. Finally, at each probe pixel the Fourier transform is computed to generate the pump frequency axis. For the 2D spectra, the real part of the Fourier transform of the time domain data is used, and the Fourier transform is computed only for values of $\tau \ge 0$ fs. Because τ cannot be exactly set to be equal to 0, τ is typically scanned starting at a slightly negative value. For each set of 2D spectra, a spectral

and phase the spectra⁴⁴. Because the data is collected in the pump-probe geometry, the peaks have absorptive lineshapes, and any apparent dispersive lineshapes are due to interference between neighboring ground state bleach/stimulated emission and excited state absorption signals⁴⁵.

2.2 All-normal dispersion photonic crystal fiber

The dispersion profile of the fiber used in this work is shown in Figure 2, as provided by NKT Photonics. The maximum dispersion wavelength is located at approximately 1020 nm. Here, the wavelength dependent dispersion parameter, D_{λ} , is related to the group velocity dispersion (GVD), β_2 , by Equation (1) shown below.

$$D_{\lambda} = -\frac{2\pi c}{\lambda^2} \beta_2 \tag{1}$$

Figure 2b shows the group delay dispersion (GDD) calculated from the dispersion profile for a 5 cm length of fiber. It should be noted that there is a sign difference between D_{λ} and β_2 ; since the fiber has normal dispersion, β_2 is positive while D_{λ} is negative. The GDD curve has a nonlinear shape indicating a non-negligible amount of higher order dispersion. Because the chirped mirrors used for pulse compression primarily correct for second order dispersion (linear chirp), the higher order dispersion is uncompensated.

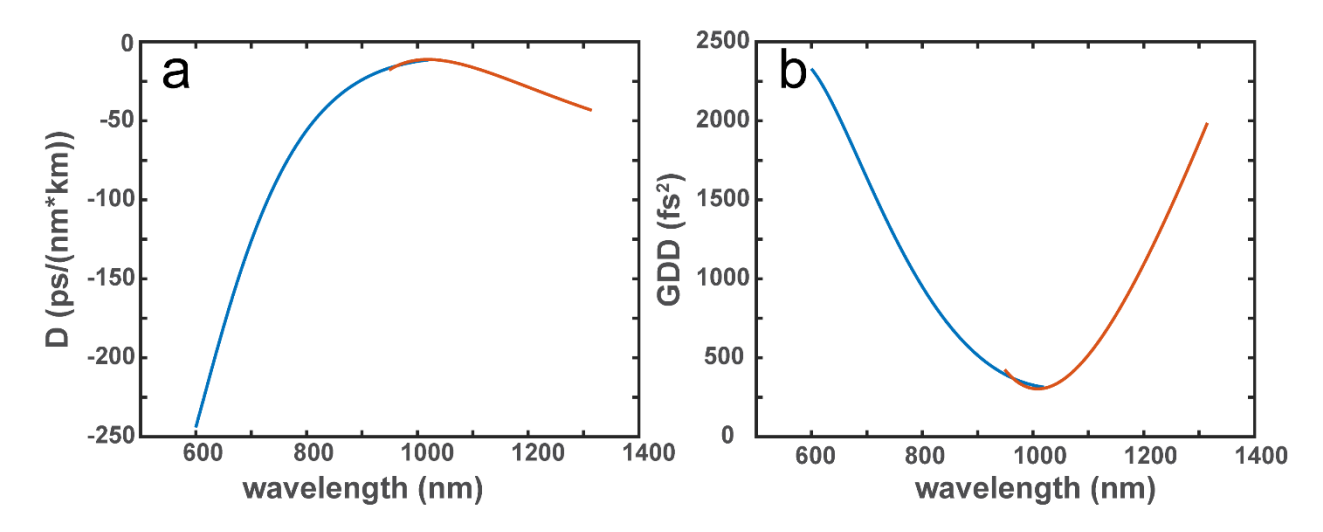


Figure 2. (a) Dispersion profile of ANDi PCF (provided by NKT Photonics). (b) Group delay dispersion of 5 cm of ANDi PCF calculated from the dispersion profile. Data from 600 – 1000 nm is shown in blue and data from 950 – 1300 nm is shown in orange.

3. Results and Discussion

3.1 Supercontinuum generation in ANDi PCF

Due to the large amount of higher order dispersion in the generated continuum, and because we use a chirped mirror compressor which compensates primarily for 2nd order dispersion, we could not compress the entire bandwidth of the supercontinuum. Therefore, we utilized and compressed two spectral regions of the supercontinuum separately: the NIR spanning 950 – 1200 nm, and the visible region covering 630 – 800 nm. To generate NIR, 3.5 nJ was focused into the fiber to generate the supercontinuum. A long-pass filter with a cutoff wavelength of 950 nm was used to set the short wavelength edge of the spectrum, while the long wavelength edge was set by the reflectivity of the chirped mirrors. To generate the visible, 14 nJ of the laser output was focused into the fiber to generate a continuum. A short-pass filter with an 800 nm cutoff wavelength was used to filter out longer wavelengths. The NIR supercontinuum along with the input Yb laser spectrum is shown in Figure 3a and the visible supercontinuum is shown in Figure 3b. Stability of the supercontinuum over the course of data collection time is shown in the Supporting Information.

For day-to-day use, the alignment into the ANDi PCF was optimized after starting up the laser and would not need to be re-aligned during over the course of running experiments with operation typically lasting 8-10 hours.

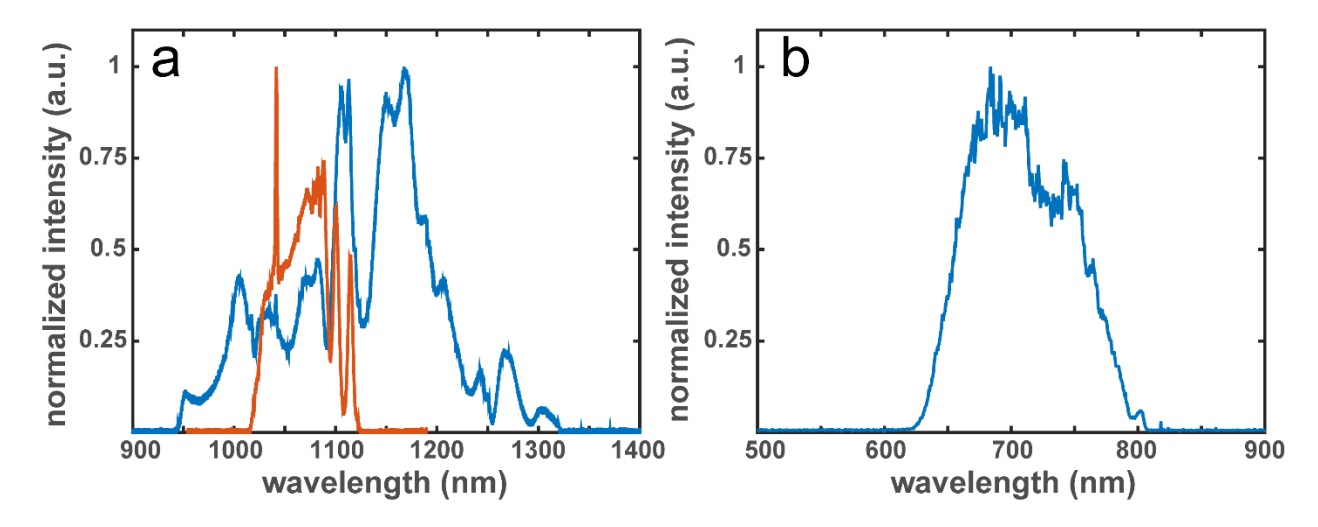


Figure 3. (a) NIR supercontinuum generated in ANDi PCF (blue) and input Yb laser spectrum (orange). The short wavelength cutoff at ~950 nm is set by the long-pass filter while the drop in intensity at ~1200 nm is due to the drop in reflectivity of the chirped mirrors. (b) Visible supercontinuum generated in ANDi PCF. The long wavelength cutoff at ~800 nm is set by the short-pass filter while the short wavelength edge of the spectrum is the extent of spectral broadening with 14 nJ input into the ANDi PCF.

3.2 Compression of supercontinuum

The large amount of higher order dispersion due to the relatively long length of the fiber meant that the chirped mirror compressor could not simultaneously compress the visible and NIR wavelength regions. For the NIR region 14 double bounces in the chirped mirror compressor produced the shortest pulse at the sample position. The pulses were characterized using an all-reflective, home-built frequency resolved optical gating (FROG) setup based on second harmonic generation (SHG)⁴⁶. In the FROG setup, the input pulse is spatially split using the edge of a square mirror. The inter-pulse delay is controlled with an optical delay line on a linear translation stage and the two pulses are focused non-collinearly into a 20 μ m thick β -BBO crystal. The second-

harmonic is frequency-resolved in a fiber-coupled spectrometer (ASEQ Instruments). The measured FROG trace of the NIR supercontinuum is shown in Figure 4a with the retrieved trace in Figure 4b; besides the asymmetry in the measured trace due to imperfect alignment in the experiment, the retrieved and measured traces show good agreement. The retrieved spectral intensity and phase are shown in Figure 4c. The phase is relatively flat and stays within < 3 radians throughout the spectrum with some small oscillation due to higher order dispersion. The retrieved temporal intensity is shown in Figure 4d. The main pulse has a full-width at half-maximum (FWHM) of 12 fs with two smaller side pulses: one with ~30 % and one with <10% of the intensity of the main pulse.

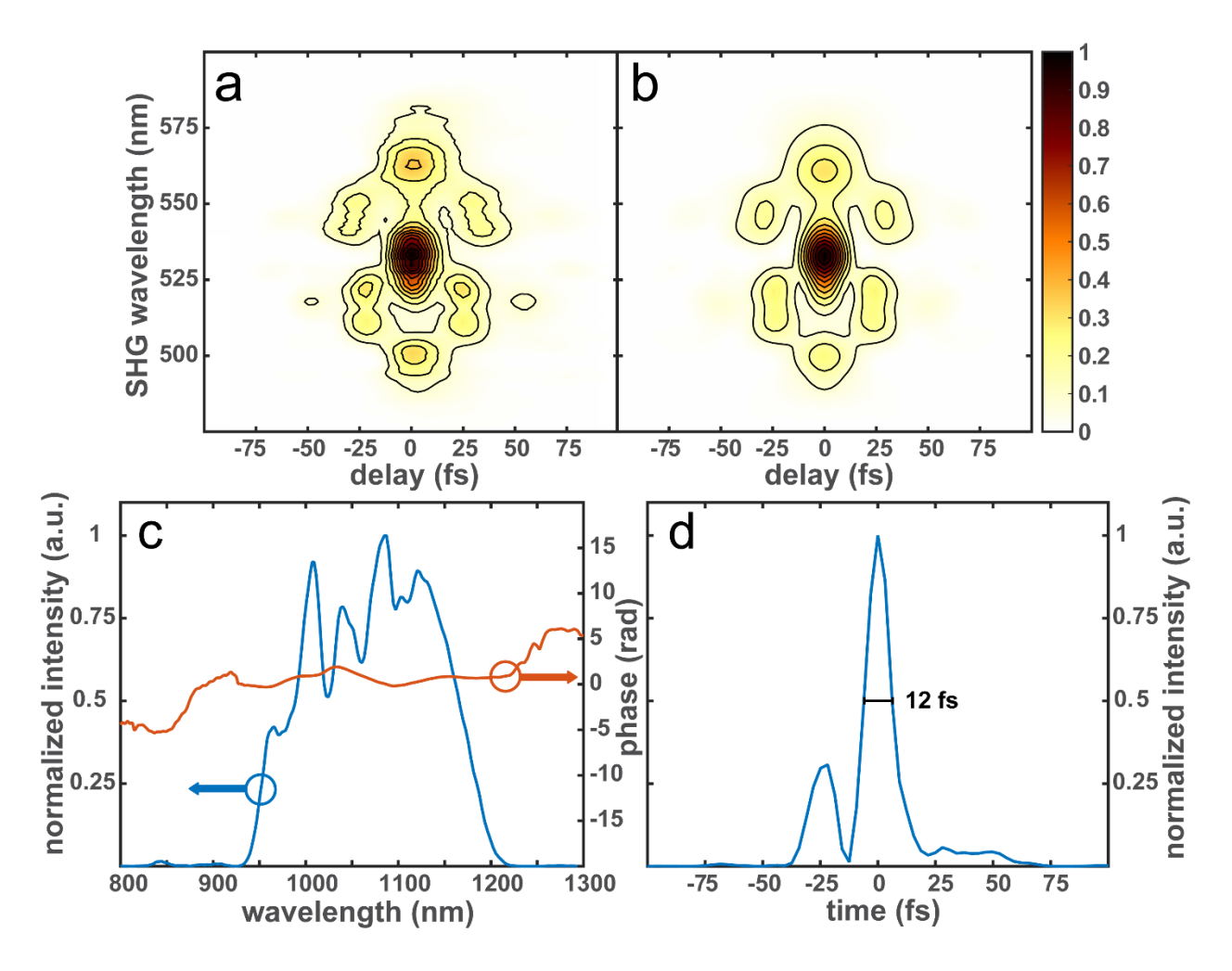


Figure 4 Characterization of NIR supercontinuum. (a) Measured SHG FROG trace. (b) Reconstructed SHG FROG trace. (c) Retrieved spectrum (blue) and phase (orange) of NIR supercontinuum. (d) Retrieved temporal intensity of NIR supercontinuum (FWHM = 12 fs).

For the visible spectral region 17 pairs of bounces in the chirped mirror compressor were required. Even though an iris aperture was used to spatially filter the second harmonic beam from the fundamental pulses after the β -BBO crystal, the small amount of leak-through was enough to saturate the detector in the FROG measurements. To overcome this, a UV bandpass filter which transmits 325-380 nm was placed after the β -BBO crystal. The measured FROG trace of the visible supercontinuum is shown in Figure 5a and shows good agreement with the retrieved trace shown in Figure 5b. The retrieved spectral intensity and phase is shown in Figure 5c. The spectral

phase stays within < 3 radians over the optical bandwidth, but also shows higher order dispersion. The effects of the higher order can be seen in the retrieved temporal intensity shown in Figure 5d which shows the main pulse with a FWHM of 18 fs and a tail extending to ~35 fs and a side pulse with a relative intensity of ~40% of the main pulse.

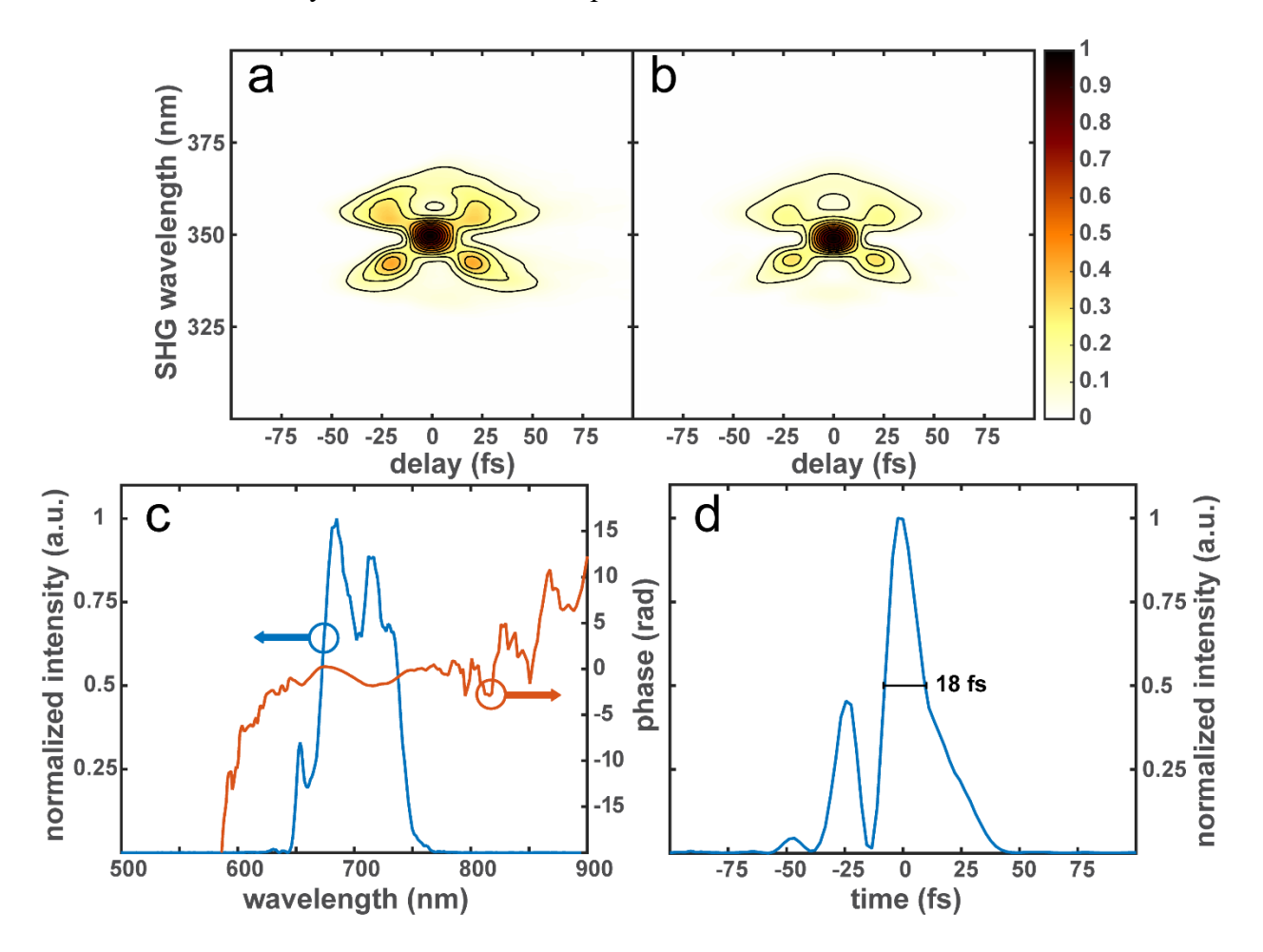


Figure 5 Characterization of visible supercontinuum. (a) Measured SHG FROG trace. (b) Reconstructed SHG FROG trace. (c) Retrieved spectrum (blue) and phase (orange) of visible supercontinuum. (d) Retrieved temporal intensity of visible supercontinuum (FWHM = 18 fs).

The major contribution of higher order dispersion comes from the fiber as shown in Figure 2b. Previous studies have shown that significant broadening of the input spectrum occurs after ~1 cm of propagation, and broadening is complete after ~3 cm of propagation in the fiber^{31,37}. Due to practical constraints from the available fiber handling equipment, the shortest segment of fiber

we were able to cleave was ~5 cm. Because the dispersion due to transmission is linearly dependent on the length of the transmissive material, using a fiber length of ~1 cm or less would greatly reduce the amount of dispersion from the fiber without sacrificing optical bandwidth or power.

3.3 Transient absorption and 2DWL spectroscopy

We demonstrated the ability to use supercontinuum generated from an ANDi PCF for ultrafast transient absorption and 2DWL spectroscopy on thin film samples comprised of mixtures of semiconducting carbon nanotubes (CNTs). Sample preparation methods are described in the Supporting Information. Figure 6a shows the absorption spectrum of a mixture of (7,6), (7,5), and (6,5) chirality nanotubes. Figure 6b shows the absorption spectrum zoomed in on the S₁ region of the nanotubes and the NIR supercontinuum overlaid which overlaps with the S₁ transitions of all 3 nanotube chiralities.

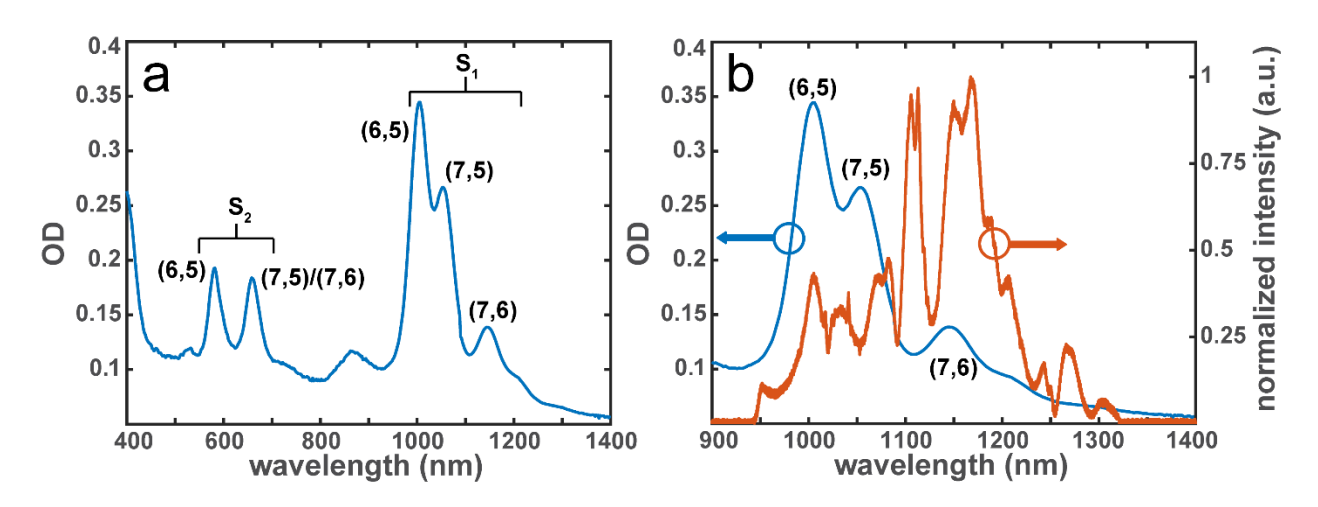


Figure 6 (a) Linear absorption spectrum of CNT film. Transitions from each nanotube chirality are labeled. (b) Zoom in of absorption spectrum highlighting the S₁ region of the three CNT chiralities (blue) with the NIR supercontinuum spectrum (orange).

For the transient absorption and 2D measurements in this work, the probe and pump pulses all have the same polarization. To collect transient absorption scans the coherence time, τ , is set

to 0 fs, and the waiting time, T, is scanned. For 2D measurements, the coherence time is scanned at a fixed waiting time to generate a single spectrum. Multiple spectra are collected at different waiting times. In the S₁ region, the coherence time was scanned from -10 fs to 400 fs in steps of 0.5 fs. Each individual τ was averaged for 500 ms before stepping to the next τ . The motor used to remove pump scatter did not remove the scatter completely. To remove the residual interference between the pump and probe, a low pass filter was used along the probe axis. Additionally, a Gaussian filter function with a 200 fs FWHM is multiplied with the interferogram before computing the Fourier transform⁴⁵. The effect of the window function on the spectra is negligible (see Supporting Information). For each set of 2D spectra collected, a spectral interferogram of the pump pulses is also collected by scanning τ and measuring the pump light. This is done to calibrate the pump wavelength axis and properly phase the data for each data set. Additionally, the spectral interferogram is processed in the same way as the 2D data so the 2D spectra can be normalized to the pump spectrum. This removes any possible distortions in the data that come from variations in the pump spectrum. For both the transient absorption and 2D measurements, the pump energy is 57 pJ and the probe is 23 pJ per pulse. The transient absorption of the SWCNT film is shown in Figure 7a with 5 main features are apparent: stimulated emission (SE) and ground state bleach (GSB) signals corresponding to bandgap nanotube transitions as well as blue-shifted excited state absorption (ESA) signals from the (7,6) and (6,5) nanotubes. The excited state absorption of the (7,5) nanotubes is obscured in the transient absorption due interference with the nearby GSB and SE signals. Fits to the GSB and SE signals in the transient absorption data are shown in the Supporting Information. The observed signals decay on similar timescales as previously studied CNT films⁴⁷ (lifetimes are not expected to be precisely the same, because exciton lifetimes are strongly dependent on film preparation conditions⁴⁸). The 2D spectra are shown in Figure 7b-f.

Each spectrum is normalized to the intensity of the GSB/SE of the (6,5) S_1 transition (peak AA) at $\lambda_{pump} = 1000$ nm, $\lambda_{probe} = 1010$ nm.

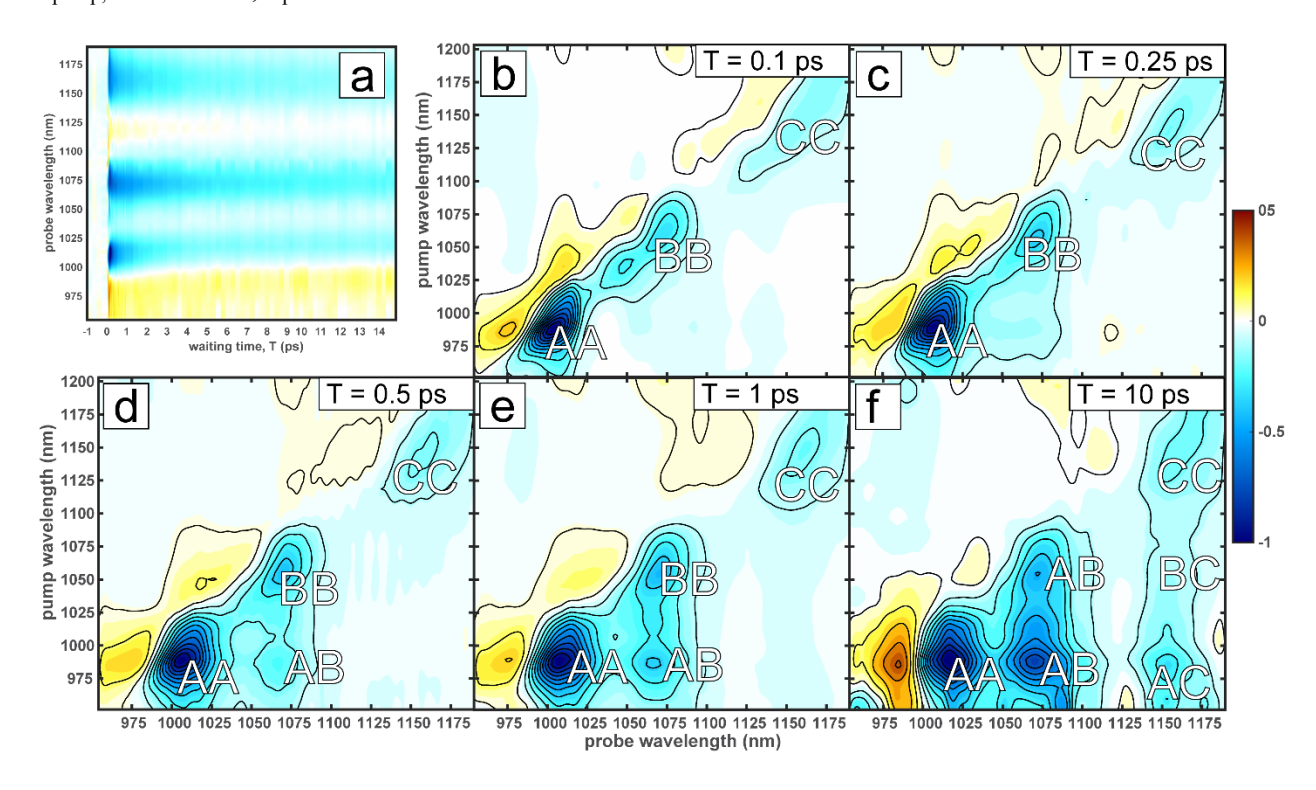


Figure 7. (a) Transient absorption spectra in the S₁ region of the CNT film with NIR supercontinuum pump and probe as a function of waiting time, T. (b-f) Broadband 2DWL spectra of the S₁ region of the CNT film with NIR supercontinuum pump and probe at different waiting times.

In the 2D spectra, peaks AA, BB, and CC correspond to the GSB/SE diagonal peaks of the (6,5), (7,5), and (7,6) chiralities, respectively, indicating that the signals are pumped and probed at the same frequency. Cross-peaks between two chiralities are labeled with two different letters. For example, peak AB corresponds to the cross-peak between the (6,5) to the (7,5) nanotubes. Only diagonal GSB/SE and cross-peak GSB/SE signals are labeled. At early waiting times, diagonal GSB and SE peaks corresponding to the S_1 transition from each of the three nanotube chiralities as well as their blue shifted ESAs are the main apparent features. At small waiting times, T = 0.1 ps and T = 0.25 ps, the peaks are elongated along the diagonal indicating inhomogeneous broadening. It should be noted that the added spectral dimension of the 2D spectra

compared to the transient absorption spectra allow for the ESA of the (7,5) nanotubes to be observed at $\lambda_{pump} = 1060$ nm, $\lambda_{probe} = 1030$ nm. As the system evolves at larger values of T, the cross-peak AB begins to appear at T = 0.5 ps indicating energy transfer from the (6,5) to (7,5) chiralities becoming more intense at T = 1 ps. Additionally, peaks AA and BB become more rounded indicating spectral diffusion as photogenerated excitons sample different energetic environments during the waiting time. At much a much longer waiting time, T = 10 ps, cross-peaks between all three nanotube chiralities are observed and peaks AA, BB, and CC show contributions of homogeneous broadening. Although the film studied here was prepared by different methods and contains different SWCNT chiralities compared to films previously studied by 2D spectroscopy³, the results qualitatively match.

To demonstrate the applicability of the visible supercontinuum generated from the ANDi PCF, we measured spectra in the S_2 region of a CNT film that has transitions covered by the optical spectrum shown in Figure 8b. The CNT film contains four main chiralities; the S_1 transitions are well resolved for the four chiralities, but the S_2 transitions of the (8,7) and (8,6) CNTs overlap at 725 nm and the (7,6) and (7,5) S_2 transitions overlap at 650 nm.

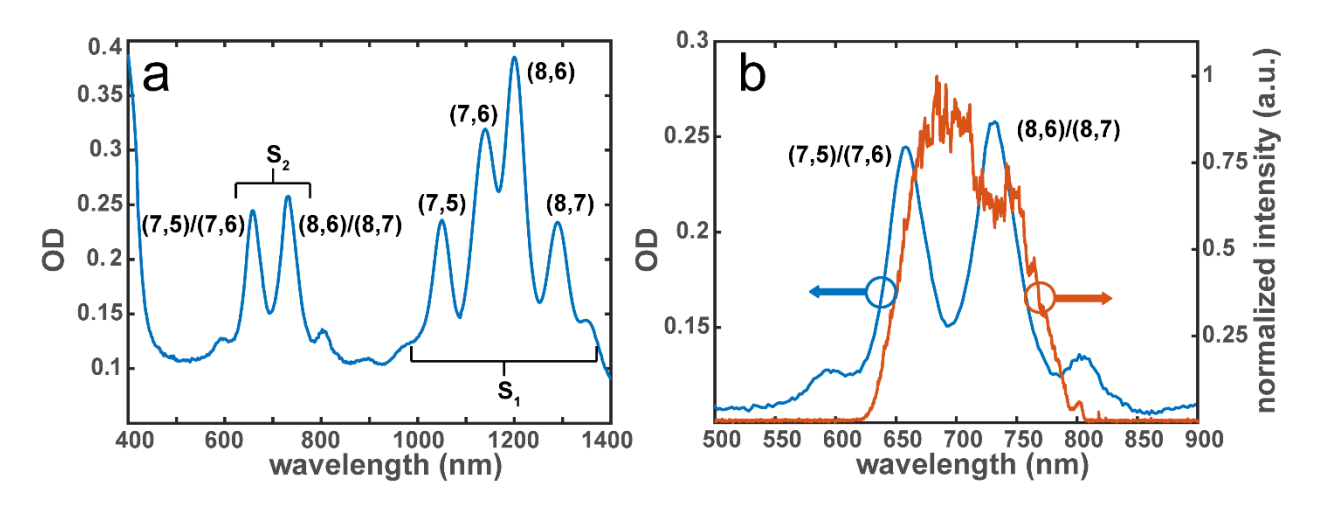


Figure 8 (a) Linear absorption spectrum of a different CNT film. Transitions from each nanotube chirality are labeled. (b) Zoom in of absorption spectrum highlighting the S₂ region of the four CNT chiralities (blue) with the visible supercontinuum spectrum (orange).

In the S_2 region, the coherence time was scanned from -10 fs to 150 fs in steps of 0.5 fs. Each τ was averaged for 500 ms and a Gaussian window with a FWHM of 5 fs 75as multiplied with the interferogram before computing the Fourier transform. The effect of the window function in the visible is negligible (see Supporting Information). The data was normalized in the same way as the NIR data. At the sample position, the pump energy was 56 pJ and the probe energy was 13 pJ per pulse. The transient absorption trace is shown in Figure 9a shows 3 main features over the detections range: GSB and SE signals at 650 nm and 725 nm, and an ESA signal at 680 nm. Fits to the GSB and SE signals of the transient absorption trace are shown in the Supporting Information. The signals decay more rapidly than the transient signals in the S_1 region, which is consistent with previous measurements³. The 2D spectra are shown in Figure 9b-f. Each spectrum is normalized to the GSB/SE peak of the (8,7) and (8,6) SWCNTs at $\lambda_{pump} = \lambda_{probe} = 725$ nm.

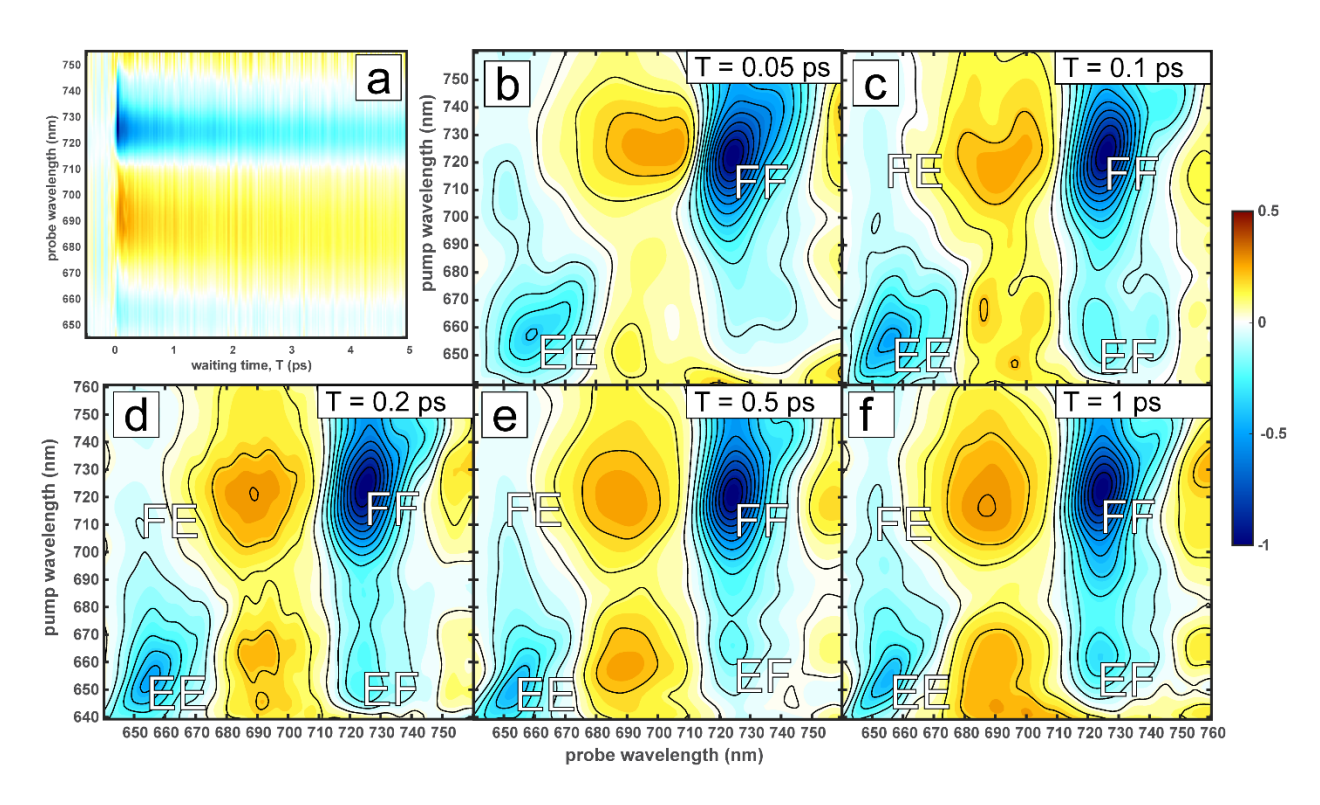


Figure 9. (a) Transient absorption spectra in the S₂ region of the CNT film with visible supercontinuum pump and probe as a function of waiting time, T. (b-f) Broadband 2DWL spectra of the S₂ region of the CNT film with visible supercontinuum pump and probe at different waiting times.

The 2DWL spectra follow the same labelling scheme as in Figure 7 with EE and FF corresponding to diagonal peaks of the (7,6)/(7,5) and (8,7)/(8,6) nanotubes, respectively. Peaks FE and EF correspond to cross-peaks between the diagonal peaks. At the earliest waiting times, both diagonal peaks and cross-peaks are present. The (7,6)/(7,5) peak (labelled EE) and the (8,7)/(8,6) peak (labelled FF) show some degree of inhomogeneous broadening indicated by elongation along the diagonal. At subsequent waiting times, cross-peak EF becomes more intense indicating energy transfer in the S₂ manifold between the (7,6)/(7,5) and (8,7)/(8,6) chiralities. The peaks also very rapidly become homogeneously broadened. Both observations are consistent with previous measurements³. Additionally, a weaker cross-peak FE appears above the diagonal at all waiting times. This signal is hypothesized to be due to a Stark shift from charge generation³. The

ability to measure high quality 2D spectra in both the visible and NIR regions show that supercontinuum in the NIR generated from ANDi PCF is a suitable light source for ultrafast spectroscopy.

3.4 Single wedge pair geometry

Finally, we demonstrate an even further simplified 2DWL spectrometer using only a Babinet-Soleil compensator to generate the pump pulse pair. This method of generating a pair of phase-locked pulses has been used previously in the mid-infrared⁴⁹. The experimental layout is shown in Figure 10. By taking the 2^{nd} wedge pair out, a pair of pulses travels along pump and probe path. As the one wedge is translated relative to the other, the inter-pulse separation, τ , is incremented as well as the absolute arrival time of the final pulse at the sample. However, the delay time between the pump and probe, T, remains fixed.

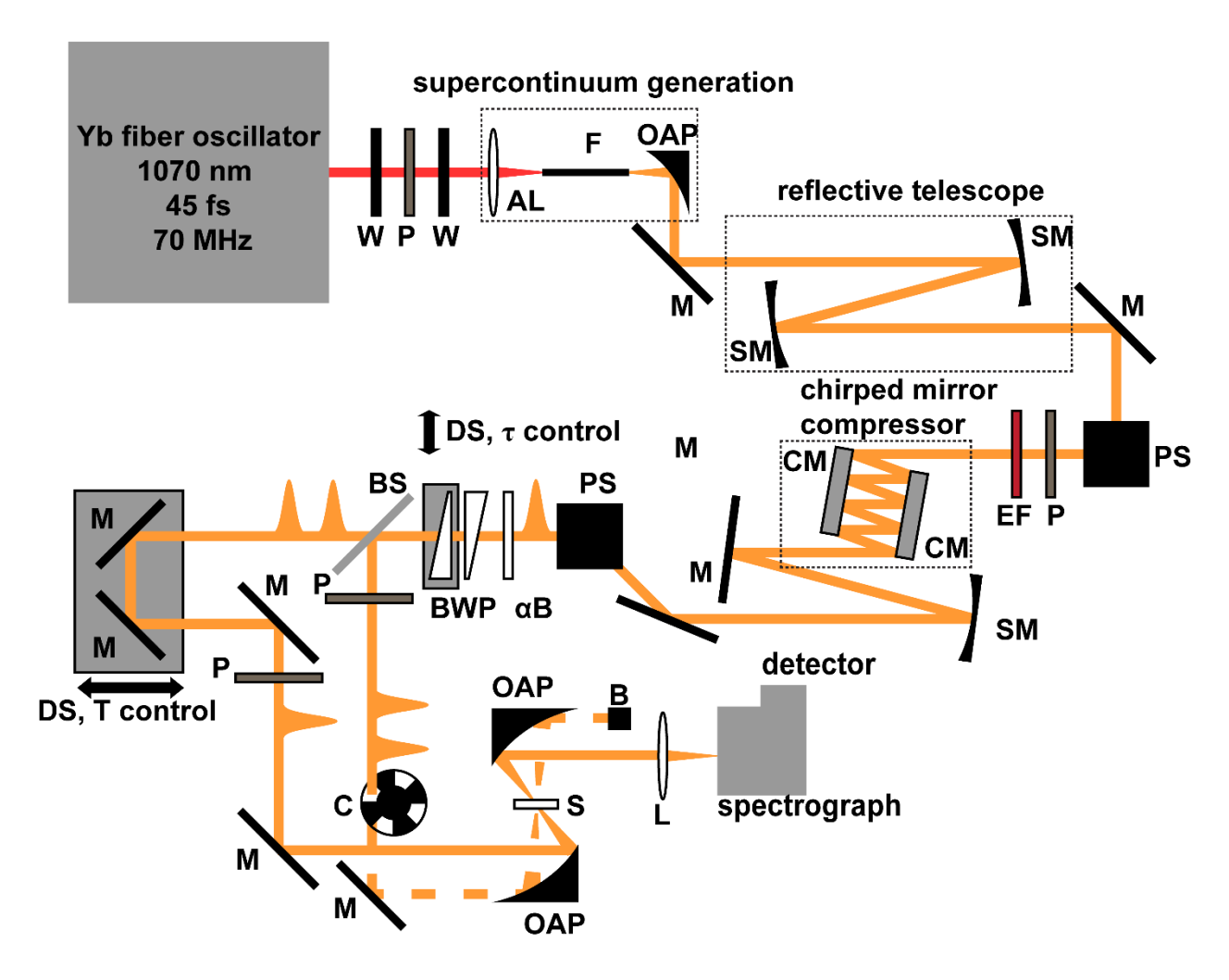


Figure 10. Diagram of experimental layout of 2DWL spectrometer using single wedge-pair geometry. W: half-wave plate, P: polarizer, AL: aspheric lens, F: ANDi PCF, OAP: 90° off-axis parabolic mirror, M: mirror, SM: spherical mirror, PS: periscope, EF: edge-pass filter, CM: chirped mirror, BS: beam splitter, αB: α-BBO plate, BWP: α-BBO wedge pair, DS: delay stage, C: optical chopper, DM: dispersive material, S: sample, B: beam block, L: lens.

In the single wedge pair geometry, the beam splitter is placed after pulse pair generation. Since the pulses are generated via birefringence, they are perpendicularly polarized. To have the pump pulses in the same polarization state, they pass through a polarizer oriented at 45°. To have a single probe pulse selected for the experiment, the probe pair passes through a polarizer oriented at 90° so that the relative polarization between the pump and probe is 45°. In practice, to have full control over the relative polarization between the pump and probe, a half-wave plate could be used

to rotate the polarization of either the pump or probe. To keep the pulse duration the same as the measurements in the previously described setup, the second pair of wedges was placed in the path of the pump beam with a fixed position so that the total amount of material is constant at every τ . With the single wedge pair, the overall amount of material changes linearly with τ . This would have a greater effect in the visible portion of the spectrum due to α -BBO having larger dispersion at shorter wavelengths. For example, scanning τ by 200 fs requires a change in thickness of α -BBO of 0.485 mm which introduces 44.7 fs² at 700 nm for the ordinary ray (33.6 fs² for the extraordinary ray). For a 10 fs Gaussian pulse centered at 700 nm, this would stretch the ordinary pulse to 16 fs and the extraordinary pulse to 13.7 fs. In the NIR, the dispersion is negligible: a both polarizations of a 10 fs pulse centered at 1100 nm would be stretched to just over 11 fs over the same scan range.

To demonstrate using the single wedge pair geometry with a supercontinuum from ANDi PCF we measure transient absorption and 2DWL spectra on the same SWCNT film in Figures 8 & 9. The results are shown in Figure 11. The transient absorption results are shown Figure 11a and the 2D results are shown in Figure 11b-f.

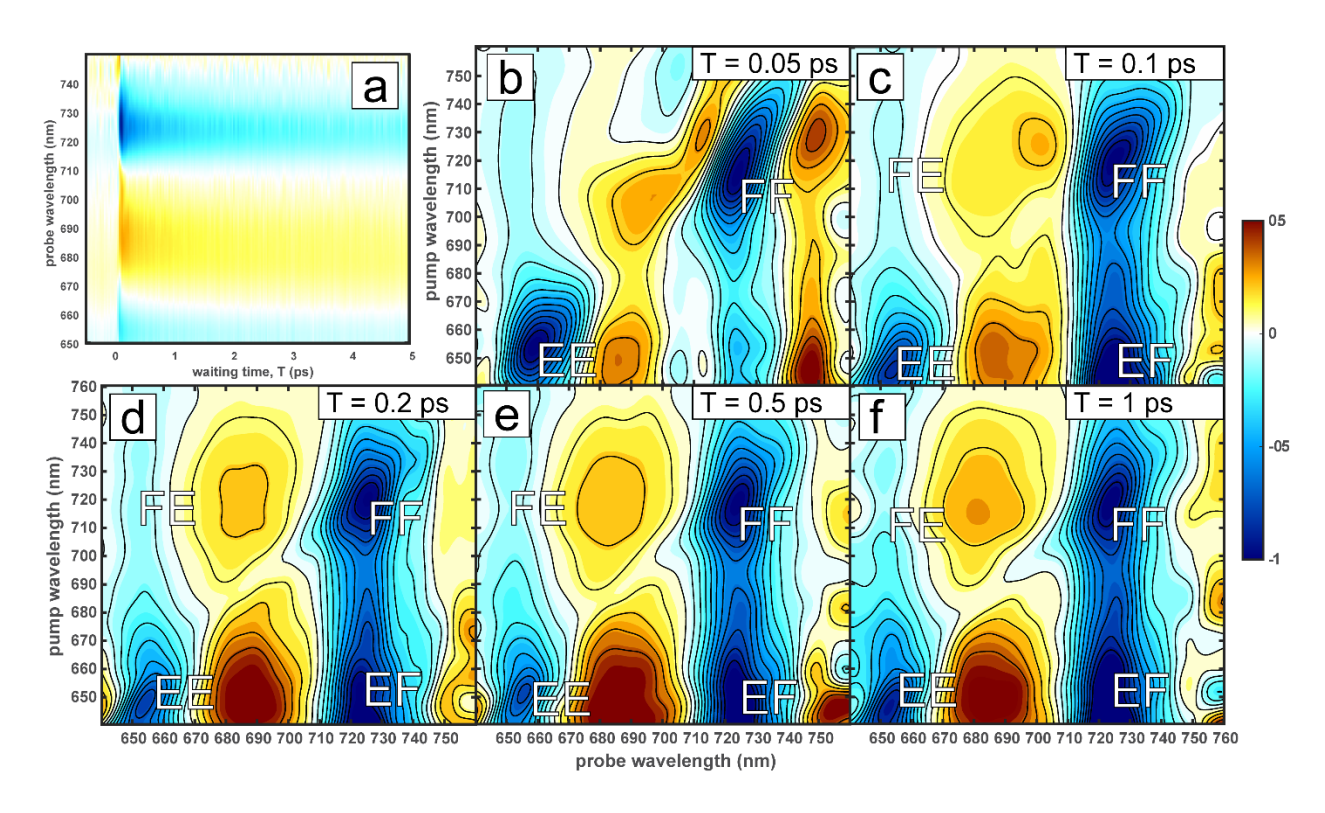


Figure 11. (a) Transient absorption spectra using the single wedge pair geometry in the S_2 region of the CNT film with visible supercontinuum pump and probe as a function of waiting time, T. (b-f) Broadband 2DWL spectra using the single wedge pair geometry in the S_2 region of the CNT film with visible supercontinuum pump and probe at different waiting times.

The data shown in Figure 11 is collected using pump pulses polarized at 45° relative to the probe pulses. This polarization scheme is used to measure electronic state lifetimes independent of reorientation dynamics in a two-dimensional sample like the CNT film measured here⁵⁰. Excellent signal-to-noise is achieved, demonstrating that the simpler experimental setup with a single wedge pair can also be used to collect high quality 2D spectra.

4. Conclusions

We have designed a broadband, ultrafast 2D electronic spectrometer that uses supercontinuum generated by pumping an ANDi PCF with a Yb fiber oscillator as the only light source. Two different experimental geometries are demonstrated: one using both a single set and

one using a double set of birefringent wedge-pairs to generate the pump pulse pair to collect 2D spectra. Compression down to sub-20 fs is achieved by only using chirped mirrors as dispersion compensation, and compression over a broader bandwidth level would be possible with a shorter length of fiber with the same compensation scheme³⁷. Even though the region of the supercontinuum near the pump wavelength has significant variations in intensity, normalization of the data to the pump and probe spectra mitigate the effect of these variations in the data yielding high quality 2D spectra. To our knowledge, this is the first example of using supercontinuum generated in ANDi PCF in multidimensional spectroscopy.

While this work shows ANDi PCF supercontinuum works very well for ensemble multidimensional spectroscopic measurements, this method of supercontinuum generation also has strong implications for broadband microscopy measurements. The ability to use a 70 Mhz repetition rate oscillator to generate ultrabroadband spectra that are highly coherent is easily adaptable to broadband nonlinear microscopies which typically rely on very high (>MHz) repetition rates to raster scan over an image. Thus, microscopy experiments analogous to transient absorption microscopy^{51–55} might be performed along with the capability of collecting spatially-resolved broadband 2DWL spectra⁵⁶.

Acknowledgements

This research was supported by the NSF CHE 1665110 and supplemented by a University-Industry Relations Industrial & Economic Development Research Grant. M.T.Z. is an owner of PhaseTech Spectroscopy, Inc., which sells 2D Visible and Infrared spectrometers and pulse shapers. We thank R. H. Goldsmith and S. K. Vanga for assistance with fiber cleaving, M. S. Arnold and J. Wang for the CNT film samples, and PhaseTech Spectroscopy, Inc. for providing the ANDi PCF.

References

- (1) Engel, G. S.; Calhoun, T. R.; Read, E. L.; Ahn, T.-K.; Mančal, T.; Cheng, Y.-C.; Blankenship, R. E.; Fleming, G. R. Evidence for Wavelike Energy Transfer through Quantum Coherence in Photosynthetic Systems. *Nature* **2007**, *446*, 782.
- Ostroumov, E. E.; Mulvaney, R. M.; Cogdell, R. J.; Scholes, G. D. Broadband 2D
 Electronic Spectroscopy Reveals a Carotenoid Dark State in Purple Bacteria. *Science (80-.)* 2013, 340 (6128), 52 LP-56.
- (3) Mehlenbacher, R. D.; McDonough, T. J.; Grechko, M.; Wu, M.-Y.; Arnold, M. S.; Zanni, M. T. Energy Transfer Pathways in Semiconducting Carbon Nanotubes Revealed Using Two-Dimensional White-Light Spectroscopy. *Nat. Commun.* 2015, 6, 6732.
- (4) Gellen, T. A.; Lem, J.; Turner, D. B. Probing Homogeneous Line Broadening in CdSe Nanocrystals Using Multidimensional Electronic Spectroscopy. *Nano Lett.* 2017, 17 (5), 2809–2815. https://doi.org/10.1021/acs.nanolett.6b05068.
- (5) Smallwood, C. L.; Cundiff, S. T. Multidimensional Coherent Spectroscopy of Semiconductors. *Laser Photon. Rev.* **2018**, *0* (0), 1800171. https://doi.org/10.1002/lpor.201800171.
- Bakulin, A. A.; Morgan, S. E.; Kehoe, T. B.; Wilson, M. W. B.; Chin, A. W.; Zigmantas,
 D.; Egorova, D.; Rao, A. Real-Time Observation of Multiexcitonic States in Ultrafast
 Singlet Fission Using Coherent 2D Electronic Spectroscopy. *Nat. Chem.* 2016, 8 (1), 16.
- (7) Wells, K. L.; Lambrev, P. H.; Zhang, Z.; Garab, G.; Tan, H.-S. Pathways of Energy Transfer in LHCII Revealed by Room-Temperature 2D Electronic Spectroscopy. *Phys. Chem. Chem. Phys.* 2014, *16* (23), 11640–11646. https://doi.org/10.1039/C4CP00876F.

- (8) Song, K.-H.; Gu, M.; Kim, M.-S.; Kwon, H.-J.; Rhee, H.; Han, H.; Cho, M. Quantum Beats and Phase Shifts in Two-Dimensional Electronic Spectra of Zinc Naphthalocyanine Monomer and Aggregate. *J. Phys. Chem. Lett.* **2015**, *6* (21), 4314–4318. https://doi.org/10.1021/acs.jpclett.5b02030.
- (9) Fuller, F. D.; Ogilvie, J. P. Experimental Implementations of Two-Dimensional Fourier Transform Electronic Spectroscopy. *Annu. Rev. Phys. Chem.* 2015, 66 (1), 667–690. https://doi.org/10.1146/annurev-physchem-040513-103623.
- (10) Tekavec, P. F.; Myers, J. A.; Lewis, K. L. M.; Ogilvie, J. P. Two-Dimensional Electronic Spectroscopy with a Continuum Probe. *Opt. Lett.* **2009**, *34* (9), 1390–1392. https://doi.org/10.1364/OL.34.001390.
- (11) Krebs, N.; Pugliesi, I.; Hauer, J.; Riedle, E. Two-Dimensional Fourier Transform Spectroscopy in the Ultraviolet with Sub-20 Fs Pump Pulses and 250–720 Nm Supercontinuum Probe. *New J. Phys.* **2013**, *15* (8), 85016.
- (12) Harel, E.; Long, P. D.; Engel, G. S. Single-Shot Ultrabroadband Two-Dimensional Electronic Spectroscopy of the Light-Harvesting Complex LH2. *Opt. Lett.* **2011**, *36* (9), 1665–1667. https://doi.org/10.1364/OL.36.001665.
- (13) Spokoyny, B.; Koh, C. J.; Harel, E. Stable and High-Power Few Cycle Supercontinuum for 2D Ultrabroadband Electronic Spectroscopy. *Opt. Lett.* **2015**, *40* (6), 1014–1017. https://doi.org/10.1364/OL.40.001014.
- Al Haddad, A.; Chauvet, A.; Ojeda, J.; Arrell, C.; van Mourik, F.; Auböck, G.; Chergui,
 M. Set-up for Broadband Fourier-Transform Multidimensional Electronic Spectroscopy.
 Opt. Lett. 2015, 40 (3), 312–315. https://doi.org/10.1364/OL.40.000312.

- (15) Ma, X.; Dostál, J.; Brixner, T. Broadband 7-Fs Diffractive-Optic-Based 2D Electronic Spectroscopy Using Hollow-Core Fiber Compression. *Opt. Express* 2016, 24 (18), 20781–20791. https://doi.org/10.1364/OE.24.020781.
- (16) Seiler, H.; Palato, S.; Schmidt, B. E.; Kambhampati, P. Simple Fiber-Based Solution for Coherent Multidimensional Spectroscopy in the Visible Regime. *Opt. Lett.* **2017**, *42* (3), 643–646. https://doi.org/10.1364/OL.42.000643.
- Mehlenbacher, R. D.; Wang, J.; Kearns, N. M.; Shea, M. J.; Flach, J. T.; McDonough, T. J.; Wu, M.-Y.; Arnold, M. S.; Zanni, M. T. Ultrafast Exciton Hopping Observed in Bare Semiconducting Carbon Nanotube Thin Films with Two-Dimensional White-Light Spectroscopy. *J. Phys. Chem. Lett.* 2016, 7 (11). https://doi.org/10.1021/acs.jpclett.6b00650.
- (18) Kearns, N. M.; Mehlenbacher, R. D.; Jones, A. C.; Zanni, M. T. Broadband 2D Electronic Spectrometer Using White Light and Pulse Shaping: Noise and Signal Evaluation at 1 and 100 KHz. *Opt. Express* **2017**, *25* (7), 7869–7883. https://doi.org/10.1364/OE.25.007869.
- (19) Berera, R.; van Grondelle, R.; Kennis, J. T. M. Ultrafast Transient Absorption
 Spectroscopy: Principles and Application to Photosynthetic Systems. *Photosynth. Res.* 2009, 101 (2), 105–118. https://doi.org/10.1007/s11120-009-9454-y.
- (20) Megerle, U.; Pugliesi, I.; Schriever, C.; Sailer, C. F.; Riedle, E. Sub-50 Fs Broadband Absorption Spectroscopy with Tunable Excitation: Putting the Analysis of Ultrafast Molecular Dynamics on Solid Ground. *Appl. Phys. B* 2009, 96 (2), 215–231. https://doi.org/10.1007/s00340-009-3610-0.
- (21) Riedle, E.; Bradler, M.; Wenninger, M.; Sailer, C. F.; Pugliesi, I. Electronic Transient

- Spectroscopy from the Deep UV to the NIR: Unambiguous Disentanglement of Complex Processes. *Faraday Discuss.* **2013**, *163* (0), 139–158. https://doi.org/10.1039/C3FD00010A.
- (22) Bradler, M.; Baum, P.; Riedle, E. Femtosecond Continuum Generation in Bulk Laser Host Materials with Sub-MJ Pump Pulses. *Appl. Phys. B* **2009**, *97* (3), 561. https://doi.org/10.1007/s00340-009-3699-1.
- (23) Dudley, J. M.; Genty, G.; Coen, S. Supercontinuum Generation in Photonic Crystal Fiber. *Rev. Mod. Phys.* **2006**, *78* (4), 1135–1184. https://doi.org/10.1103/RevModPhys.78.1135.
- (24) Genty, G.; Coen, S.; Dudley, J. M. Fiber Supercontinuum Sources (Invited). *J. Opt. Soc. Am. B* **2007**, *24* (8), 1771–1785. https://doi.org/10.1364/JOSAB.24.001771.
- (25) Gu, X.; Xu, L.; Kimmel, M.; Zeek, E.; O'Shea, P.; Shreenath, A. P.; Trebino, R.; Windeler, R. S. Frequency-Resolved Optical Gating and Single-Shot Spectral Measurements Reveal Fine Structure in Microstructure-Fiber Continuum. *Opt. Lett.* 2002, 27 (13), 1174–1176. https://doi.org/10.1364/OL.27.001174.
- (26) Gu, X.; Kimmel, M.; Shreenath, A. P.; Trebino, R.; Dudley, J. M.; Coen, S.; Windeler, R. S. Experimental Studies of the Coherence of Microstructure-Fiber Supercontinuum. *Opt. Express* 2003, *11* (21), 2697–2703. https://doi.org/10.1364/OE.11.002697.
- (27) Corwin, K. L.; Newbury, N. R.; Dudley, J. M.; Coen, S.; Diddams, S. A.; Weber, K.; Windeler, R. S. Fundamental Noise Limitations to Supercontinuum Generation in Microstructure Fiber. *Phys. Rev. Lett.* 2003, 90 (11), 113904. https://doi.org/10.1103/PhysRevLett.90.113904.

- (28) Hilligsøe, K. M.; Andersen, T. V.; Paulsen, H. N.; Nielsen, C. K.; Mølmer, K.; Keiding, S.; Kristiansen, R.; Hansen, K. P.; Larsen, J. J. Supercontinuum Generation in a Photonic Crystal Fiber with Two Zero Dispersion Wavelengths. *Opt. Express* 2004, *12* (6), 1045–1054. https://doi.org/10.1364/OPEX.12.001045.
- (29) von Vacano, B.; Wohlleben, W.; Motzkus, M. Actively Shaped Supercontinuum from a Photonic Crystal Fiber for Nonlinear Coherent Microspectroscopy. *Opt. Lett.* **2006**, *31* (3), 413–415. https://doi.org/10.1364/OL.31.000413.
- (30) Higgins, K.; Calhoun, T. R. Compressed Supercontinuum Probe for Transient Absorption Microscopy. *Opt. Lett.* **2018**, *43* (8), 1750–1753. https://doi.org/10.1364/OL.43.001750.
- (31) Heidt, A. M.; Hartung, A.; Bosman, G. W.; Krok, P.; Rohwer, E. G.; Schwoerer, H.; Bartelt, H. Coherent Octave Spanning Near-Infrared and Visible Supercontinuum Generation in All-Normal Dispersion Photonic Crystal Fibers. *Opt. Express* **2011**, *19* (4), 3775–3787. https://doi.org/10.1364/OE.19.003775.
- (32) Heidt, A. M. Pulse Preserving Flat-Top Supercontinuum Generation in All-Normal Dispersion Photonic Crystal Fibers. *J. Opt. Soc. Am. B* **2010**, *27* (3), 550–559. https://doi.org/10.1364/JOSAB.27.000550.
- (33) Sukhoivanov, I. A.; Iakushev, S. O.; Shulika, O. V; Andrade-Lucio, J. A.; Díez, A.; Andrés, M. Supercontinuum Generation at 800 Nm in All-Normal Dispersion Photonic Crystal Fiber. *Opt. Express* 2014, 22 (24), 30234–30250. https://doi.org/10.1364/OE.22.030234.
- (34) Tu, H.; Liu, Y.; Turchinovich, D.; Boppart, S. A. Compression of Fiber Supercontinuum Pulses to the Fourier-Limit in a High-Numerical-Aperture Focus. *Opt. Lett.* **2011**, *36* (12),

- 2315–2317. https://doi.org/10.1364/OL.36.002315.
- (35) Liu, Y.; Tu, H.; Boppart, S. A. Wave-Breaking-Extended Fiber Supercontinuum Generation for High Compression Ratio Transform-Limited Pulse Compression. *Opt. Lett.* 2012, 37 (12), 2172–2174. https://doi.org/10.1364/OL.37.002172.
- (36) Demmler, S.; Rothhardt, J.; Heidt, A. M.; Hartung, A.; Rohwer, E. G.; Bartelt, H.; Limpert, J.; Tünnermann, A. Generation of High Quality, 1.3 Cycle Pulses by Active Phase Control of an Octave Spanning Supercontinuum. *Opt. Express* **2011**, *19* (21), 20151–20158. https://doi.org/10.1364/OE.19.020151.
- (37) Heidt, A. M.; Rothhardt, J.; Hartung, A.; Bartelt, H.; Rohwer, E. G.; Limpert, J.; Tünnermann, A. High Quality Sub-Two Cycle Pulses from Compression of Supercontinuum Generated in All-Normal Dispersion Photonic Crystal Fiber. *Opt. Express* 2011, *19* (15), 13873–13879. https://doi.org/10.1364/OE.19.013873.
- (38) Shim, S.-H.; Zanni, M. T. How to Turn Your Pump–probe Instrument into a Multidimensional Spectrometer: 2D IR and Vis Spectroscopiesvia Pulse Shaping. *Phys. Chem. Chem. Phys.* 2009, 11 (5), 748–761. https://doi.org/10.1039/B813817F.
- (39) Brida, D.; Manzoni, C.; Cerullo, G. Phase-Locked Pulses for Two-Dimensional Spectroscopy by a Birefringent Delay Line. *Opt. Lett.* **2012**, *37* (15), 3027–3029. https://doi.org/10.1364/OL.37.003027.
- (40) Wasylczyk, P.; Wasilewski, W.; Radzewicz, C. Single-Shot Autocorrelator Based on a Babinet Compensator. *Rev. Sci. Instrum.* 2004, 75 (7), 2482–2484. https://doi.org/10.1063/1.1765763.

- (41) Pawłowska, M.; Ozimek, F.; Fita, P.; Radzewicz, C. Collinear Interferometer with
 Variable Delay for Carrier-Envelope Offset Frequency Measurement. *Rev. Sci. Instrum.* 2009, 80 (8), 83101. https://doi.org/10.1063/1.3197404.
- (42) Tu, H.; Liu, Y.; Liu, X.; Turchinovich, D.; Lægsgaard, J.; Boppart, S. A. Nonlinear Polarization Dynamics in a Weakly Birefringent All-Normal Dispersion Photonic Crystal Fiber: Toward a Practical Coherent Fiber Supercontinuum Laser. *Opt. Express* 2012, 20 (2), 1113–1128. https://doi.org/10.1364/OE.20.001113.
- (43) Réhault, J.; Maiuri, M.; Oriana, A.; Cerullo, G. Two-Dimensional Electronic Spectroscopy with Birefringent Wedges. *Rev. Sci. Instrum.* **2014**, *85* (12), 123107. https://doi.org/10.1063/1.4902938.
- (44) Helbing, J.; Hamm, P. Compact Implementation of Fourier Transform Two-Dimensional IR Spectroscopy without Phase Ambiguity. *J. Opt. Soc. Am. B* **2011**, *28* (1), 171–178. https://doi.org/10.1364/JOSAB.28.000171.
- (45) Hamm, P.; Zanni, M. Concepts and Methods of 2D Infrared Spectroscopy; Cambridge University Press, 2011.
- (46) Trebino, R.; DeLong, K. W.; Fittinghoff, D. N.; Sweetser, J. N.; Krumbügel, M. A.; Richman, B. A.; Kane, D. J. Measuring Ultrashort Laser Pulses in the Time-Frequency Domain Using Frequency-Resolved Optical Gating. *Rev. Sci. Instrum.* 1997, 68 (9), 3277–3295. https://doi.org/10.1063/1.1148286.
- (47) Mehlenbacher, R. D.; Wu, M.-Y.; Grechko, M.; Laaser, J. E.; Arnold, M. S.; Zanni, M. T. Photoexcitation Dynamics of Coupled Semiconducting Carbon Nanotube Thin Films.
 Nano Lett. 2013, 13 (4), 1495–1501.

- (48) Wang, J.; Shea, M. J.; Flach, J. T.; McDonough, T. J.; Way, A. J.; Zanni, M. T.; Arnold,
 M. S. Role of Defects as Exciton Quenching Sites in Carbon Nanotube Photovoltaics. *J. Phys. Chem. C* 2017, *121* (15), 8310–8318.
- (49) Réhault, J.; Borrego-Varillas, R.; Oriana, A.; Manzoni, C.; Hauri, C. P.; Helbing, J.;
 Cerullo, G. Fourier Transform Spectroscopy in the Vibrational Fingerprint Region with a
 Birefringent Interferometer. Opt. Express 2017, 25 (4), 4403–4413.
 https://doi.org/10.1364/OE.25.004403.
- (50) Mehlenbacher, R. D.; McDonough, T. J.; Kearns, N. M.; Shea, M. J.; Joo, Y.; Gopalan, P.; Arnold, M. S.; Zanni, M. T. Polarization-Controlled Two-Dimensional White-Light Spectroscopy of Semiconducting Carbon Nanotube Thin Films. *J. Phys. Chem. C* 2016, 120 (30). https://doi.org/10.1021/acs.jpcc.6b04961.
- (51) Staleva, H.; Hartland, G. V. Transient Absorption Studies of Single Silver Nanocubes. *J. Phys. Chem. C* **2008**, *112* (20), 7535–7539. https://doi.org/10.1021/jp801550x.
- (52) Wan, Y.; Guo, Z.; Zhu, T.; Yan, S.; Johnson, J.; Huang, L. Cooperative Singlet and Triplet Exciton Transport in Tetracene Crystals Visualized by Ultrafast Microscopy. *Nat. Chem.* **2015**, *7* (10), 785.
- (53) Fischer, M. C.; Wilson, J. W.; Robles, F. E.; Warren, W. S. Invited Review Article: Pump-Probe Microscopy. *Rev. Sci. Instrum.* **2016**, *87* (3), 31101. https://doi.org/10.1063/1.4943211.
- (54) Cating, E. E. M.; Pinion, C. W.; Christesen, J. D.; Christie, C. A.; Grumstrup, E. M.; Cahoon, J. F.; Papanikolas, J. M. Probing Intrawire, Interwire, and Diameter-Dependent Variations in Silicon Nanowire Surface Trap Density with Pump–Probe Microscopy.

- Nano Lett. **2017**, 17 (10), 5956–5961. https://doi.org/10.1021/acs.nanolett.7b01876.
- (55) Gabriel, M. M.; Kirschbrown, J. R.; Christesen, J. D.; Pinion, C. W.; Zigler, D. F.; Grumstrup, E. M.; Mehl, B. P.; Cating, E. E. M.; Cahoon, J. F.; Papanikolas, J. M. Direct Imaging of Free Carrier and Trap Carrier Motion in Silicon Nanowires by Spatially-Separated Femtosecond Pump–Probe Microscopy. *Nano Lett.* 2013, *13* (3), 1336–1340. https://doi.org/10.1021/nl400265b.
- (56) Jones, A. C.; Kearns, N. M.; Ho, J.-J.; Flach, J. T.; Zanni, M. T. Imaging the Structures and Energetics of Singlet Fission Microcrystals with 2D White-Light (2DWL)

 Microscopy. *Submitted* **2018**.

TOC Graphic

